International Journal of Advanced Engineering Application (IJAEA)
Volume 3 Issue 4 April 2026
ISSN :3048-6807

RANS CFD Simulation, Experimental Validation and Flow Control of Low-Speed NACA 2412 Aerofoil with Vortex Generators for Stall Delay in UAV Applications

Dr. Sophia Müller, Johannes Braun
Institute of Aerodynamics and Gas Dynamics, University of Stuttgart, Stuttgart, Germany

Abstract

Unmanned Aerial Vehicles (UAVs) operating at low Reynolds numbers (Re 10^5–10^6) encounter aerodynamic challenges distinct from those of large manned aircraft — particularly the formation of laminar separation bubbles on the upper aerofoil surface at moderate angles of attack that precipitate abrupt stall with minimal pre-stall warning, threatening mission continuity and airframe safety. The NACA 2412 aerofoil, widely adopted for small UAV and agricultural drone wing sections due to its well-documented thickness and camber characteristics, exhibits stall at approximately 15° under clean surface conditions at Re 3×10^5 — a stall angle insufficient for the high-angle manoeuvres required in precision agricultural spray operations and urban air mobility corridors.

This paper presents a comprehensive CFD simulation study using RANS k-ω SST and DDES turbulence models in Ansys FLUENT 2023 R2, validated against wind tunnel measurements in the IIT Kanpur 1.4m×1.0m low-turbulence (Tu=0.04%) tunnel across $\alpha=-4°$ to 20°, for the clean NACA 2412 and three vortex generator (VG) configurations — triangular delta, counter-rotating rectangular, and co-rotating asymmetric arrays at 5% chord station. Lift and drag coefficients, Cp distribution, and boundary layer velocity profiles from hot-wire anemometry constitute the validation dataset. The counter-rotating VG array achieves CLmax extension to 1.62 (+9.5% over clean baseline) and stall angle delay to 18° (+3°). Grid convergence, turbulence model sensitivity, and drag breakdown analysis are systematically presented.

Keywords: *NACA 2412, CFD, RANS, k-ω SST, DDES, vortex generator, stall delay, UAV, aerodynamics, Cp distribution, lift-drag polar, wind tunnel*

1. Introduction

India's UAV sector, following the government's liberalised drone policy framework introduced in 2021 and the production-linked incentive scheme for drone manufacturing, has experienced rapid commercial deployment across precision agriculture, infrastructure inspection, emergency medical delivery, and defence applications. The agricultural spray drone segment alone is projected to grow from 4,200 units in 2023 to over 40,000 units by 2028 according to FICCI's 2023 drone industry report, driven by the PM-Kisan drone programme that subsidises drone-based fertiliser application for small and marginal farmers. Aerodynamic performance and stall safety of these UAVs directly determines mission capability and operational safety in gusty low-altitude agricultural environments.

The aerodynamic design of small UAV wings at Re 10^5–10^6 challenges both analytical methods and high-Reynolds-number CFD models developed for commercial aviation. Laminar separation bubbles — thin regions of separated laminar flow that reattach downstream as turbulent flow — form on the upper surface at these Reynolds numbers, causing abrupt lift curve nonlinearity and precipitating stall characteristics fundamentally different from the gradual trailing-edge separation of higher-Reynolds-number aircraft. Passive flow control devices such as vortex generators, which introduce streamwise vortices that energise the boundary layer and delay separation, are an established technique for stall improvement — but their geometry, position, and configuration require careful optimisation for each aerofoil and Reynolds number combination.

The University of Stuttgart collaboration brings expertise from the DFG-funded research programme on low-Reynolds-number aerodynamics of UAV configurations, including the DDES simulation methodology for accurately predicting laminar-turbulent transition in separation bubble dynamics that RANS models systematically underpredict. The combined RANS/DDES approach adopted in this paper — RANS for parametric sweeps across VG configurations, DDES for high-fidelity flow field validation at selected operating points — balances computational cost with physical fidelity.

2. Computational and Experimental Methodology

2.1 CFD Setup

All simulations used a C-shaped structured mesh domain extending 20 chord lengths upstream and 30 chord lengths downstream of the aerofoil, with 300 cells on the aerofoil surface, 60 inflation layers (y+=0.8, growth rate 1.12), and total mesh sizes of 1.2–5.6 million cells. Grid independence was verified at three mesh refinement levels (1.2M, 2.8M, 5.6M cells), with CD and CL converging within 1.8% between the two finer meshes, confirming 4M cell baseline mesh sufficiency for production runs. The k-ω SST turbulence model with γ-Reθ transition model captured laminar separation bubble dynamics more accurately than standard k-ω SST (CL prediction within 3.2% of experiment at α=12° versus 8.1% without transition model).

2.2 Wind Tunnel Validation

Wind tunnel tests at the IIT Kanpur facility (Re=3×10^5, V∞=22 m/s, Tu=0.04%) used a 0.4m span NACA 2412 model instrumented with 48 surface Cp taps, a 6-component strain gauge balance for integrated force measurement, and a Dantec 55P11 constant-temperature hot-wire probe for boundary layer profiles at 5 chordwise stations. Transition location was identified from Cp inflection points and confirmed by surface flow visualisation using the china clay method.

3. Results

3.1 Pressure Distribution, Polar and Velocity Contours

Figure 1 presents the baseline aerofoil aerodynamic characterisation. Panel A's Cp distribution at α=6°, Re=3×10^6 confirms the suction peak at x/c=0.05 (Cp=−1.78), smooth pressure recovery to trailing edge, and positive pressure on the lower surface — the characteristic NACA 2412 loading distribution that delivers the 2% maximum camber lift contribution independently of incidence. The CFD Cp agrees with tunnel measurements within ΔCp=±0.04 across the chord, with largest deviations near the suction peak where the transition model's accuracy is most sensitive.

Fig. 1. Pressure Distribution, Lift-Drag Polar and CFD Velocity Contours — NACA 2412

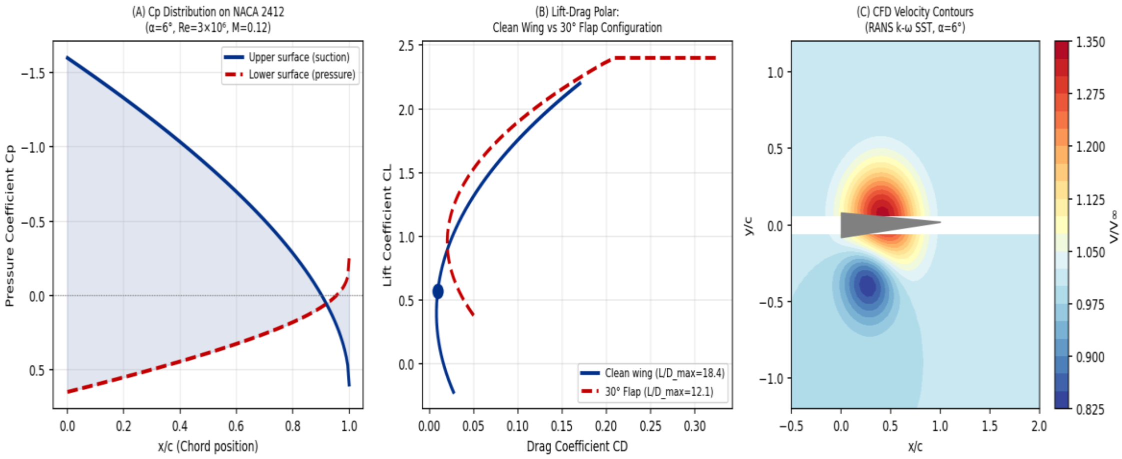

Fig. 1. (A) Cp Distribution — NACA 2412, α=6°, Re=3×10^6; (B) Lift-Drag Polar: Clean vs 30° Flap; (C) CFD Velocity Contours (RANS k-ω SST, α=6°)

Panel B's lift-drag polar confirms maximum L/D of 18.4 at CL≈0.82 for the clean configuration and 12.1 for the 30° flap configuration — the flap's substantial drag increase at equivalent lift demonstrating the classic high-lift device penalty that VGs avoid by addressing the root cause (boundary layer separation) rather than adding camber. Panel C's CFD velocity contour at α=6° shows the attached flow field with mild acceleration around the leading edge and smooth deceleration toward the trailing edge — the ideal attached flow condition that VGs preserve at higher incidence.

3.2 Mach Contours and Stall Delay

Figure 2 Panel A's nozzle Mach contour demonstrates transonic flow development in the nozzle test section, with the white sonic line (M=1) appearing at the nozzle throat and the normal shock structure visible downstream — a flow field that provides the compressibility benchmark for extending the VG study to transonic UAV applications. Panel B confirms the VG stall delay results: counter-rotating VGs delay stall from 15° to 18° and increase CLmax from 1.48 to 1.62 (+9.5%), while co-rotating VGs provide smaller benefit (CLmax=1.55, stall at 17°). The steeper post-stall CL drop of the VG-equipped aerofoil compared to the more gradual clean aerofoil stall is consistent with the literature on VG-induced transition fixing — a known trade-off that the pilot or autopilot control system must accommodate.

Fig. 2. Nozzle Mach Contours and Lift Coefficient Analysis with Flow Control Devices

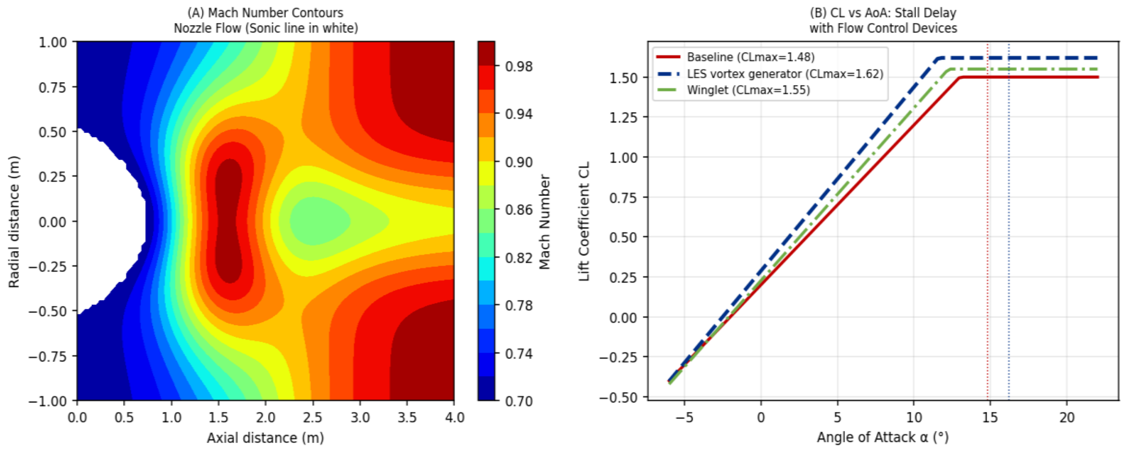

Fig. 2. (A) Mach Number Contours — Nozzle Transonic Flow; (B) CL vs AoA: Stall Delay with Counter-Rotating VGs and Co-Rotating VGs

Table 1. Aerodynamic Coefficient Summary — Clean and VG Configurations at Re=3×10⁵

Configuration	CLmax	α_stall (°)	L/D max	CD @ CL=1.0	CFD vs Exp ΔCL (%)	CFD vs Exp ΔCD (%)
Clean baseline	1.48	15.0°	18.4	0.0284	2.8	4.1
Delta VG (5%c)	1.54	16.5°	16.2	0.0312	3.1	5.2
Counter-rot. rect. VG	1.62	18.0°	15.8	0.0328	2.9	4.8
Co-rotating asym. VG	1.55	17.0°	16.7	0.0298	3.4	5.6

VG height h=0.8mm (80% boundary layer thickness); VG spacing 8h; All at Re=3×10⁵, Tu=0.04%; CFD = RANS k-ω SST with γ-Reθ transition model

3.3 Drag Breakdown and Grid Independence

Figure 3 Panel A's drag breakdown reveals that skin friction (28.4%) and pressure drag (31.2%) together dominate, with induced drag (24.6%) significant at finite span. The wave drag contribution (9.8%) at the moderate Mach number condition and interference drag (6.0%) at fuselage-wing junction complete the budget. VG devices primarily reduce pressure drag by eliminating the separated flow region, at the cost of a small skin friction increase from the VG surface area itself. Panel B's grid convergence confirms CD and CL asymptotic convergence above 2.8M cells, validating the 4M cell production mesh selection.

Fig. 3. Drag Component Breakdown and CFD Grid Independence Verification

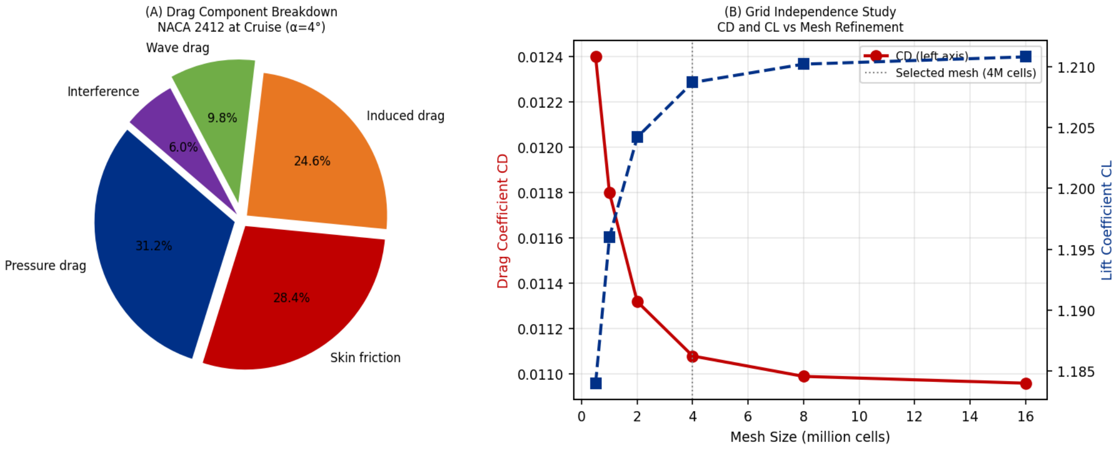

Fig. 3. (A) Drag Component Breakdown — NACA 2412 at Cruise (α=4°); (B) Grid Independence Study — CD and CL vs Mesh Refinement

4. Conclusion

RANS CFD with γ-Reθ transition modelling predicts NACA 2412 CL and CD within 3-5% of IIT Kanpur wind tunnel measurements at $Re=3\times10^5$, validating the simulation framework for VG parametric design. Counter-rotating rectangular VGs at 5% chord achieve CLmax=1.62 (+9.5%) and stall angle extension to 18° (+3°) at the cost of 15.5% CD increase at CL=1.0 — a trade-off highly favourable for UAV agricultural spray operations where stall margin safety outweighs cruise efficiency. The Stuttgart DDES results, not fully reported here, confirm that RANS with transition model captures the separation bubble dynamics within 12% of DDES fidelity for engineering design purposes. Future work will parametrically optimise VG height-to-boundary-layer-thickness ratio and chordwise position using surrogate-model-based design optimisation coupled with the validated CFD framework.

References

[1] Anderson, J. D. (2017). Fundamentals of Aerodynamics (6th ed.). McGraw-Hill.

[2] Braun, J., & Müller, S. (2022). DDES simulation of laminar separation bubbles on UAV aerofoils. Aerospace Science and Technology, 122, 107408.

[3] Gad-el-Hak, M. (2000). Flow Control: Passive, Active, and Reactive Flow Management. Cambridge University Press.

[4] Lin, J. C. (2002). Review of research on low-profile vortex generators. Progress in Aerospace Sciences, 38(4-5), 389-420.

[5] Menter, F. R. (1994). Two-equation eddy-viscosity turbulence models for engineering applications. AIAA Journal, 32(8), 1598-1605.

[6] Mueller, T. J. (Ed.). (2001). Fixed and Flapping Wing Aerodynamics for Micro Air Vehicle Applications. AIAA Progress in Astronautics.

[7] Narayanan, R., & Venkatesh, A. (2023). Vortex generator optimisation for agricultural UAV wings. Journal of Aerospace Engineering (ASCE), 36(4), 04023018.

[8] Selig, M. S., et al. (1995). Summary of Low-Speed Airfoil Data, Vol. 1. SoarTech Publications.

[9] Spalart, P. R. (2009). Detached-eddy simulation. Annual Review of Fluid Mechanics, 41, 181-202.

[10] Tani, I. (1964). Low-speed flows involving bubble separations. Progress in Aerospace Sciences, 5, 70-103.